A laboratory study to estimate pore geometric parameters of sandstones using complex conductivity and nuclear magnetic resonance for permeability prediction

In preparation for: Water Resources Research

Gordon Osterman[1], Kristina Keating[1], Andrew Binley[2], Lee Slater[1]

[1] Department of Earth and Environmental Sciences, Rutgers University-Newark, Newark, NJ

[2] Lancaster Environment Centre, Lancaster University, Lancaster, UK

Key Points:

- Complex conductivity and NMR predict the parameters of the Katz and Thompson permeability model
- A joint complex conductivity and NMR model accurately predicts permeability for sandstones
- Prediction uncertainty cannot be attributed to iron (III) content variability alone

Index Terms: 1835: Hydrogeophysics; 3914: Electrical properties; 3929: NMR

Key words: Permeability, complex conductivity, nuclear magnetic resonance, induced polarization

Abstract:

We estimate parameters from the Katz and Thompson permeability model using laboratory complex electrical conductivity (CC) and nuclear magnetic resonance (NMR) data to build permeability models parameterized with geophysical measurements. We use the Katz and Thompson model based on the characteristic hydraulic length scale, determined from mercury injection capillary pressure estimates of pore throat size, and the intrinsic formation factor, determined from multi-salinity conductivity measurements, for this purpose. Two new permeability models are tested, one based on CC data and another that incorporates CC and NMR data. From measurements made on forty-five sandstone cores collected from fifteen different formations, we evaluate how well the CC relaxation time and the NMR transverse relaxation times compare to the characteristic hydraulic length scale and how well the formation factor estimated from CC parameters compares to the intrinsic formation factor. We find: (1) the NMR transverse relaxation time models the characteristic hydraulic length scale more accurately than the CC relaxation time (R^2 of 0.69 and 0.39 and normalized root mean square errors (NRMSE) of 0.16 and 0.20, respectively); (2) the CC estimated formation factor is well correlated with the intrinsic formation factor (NRMSE=0.23). We demonstrate that that permeability estimates from the joint-NMR-CC model (NRMSE=0.13) compare favorably to estimates from the Katz and Thompson model (NRMSE=0.074). This model advances the capability of the Katz and Thompson model by employing parameters measureable in the field giving it the potential to more accurately estimate permeability using geophysical measurements than are currently possible.

1. Introduction:

Accurate estimation of permeability (k) is critical for hydrogeological modeling due to its high degree of variability, even within a single formation, and its influence on the flow of water in hydrogeological systems. Estimating the spatial distribution of k in the field is a difficult and time-consuming task requiring the use of pumping tests and/or slug tests at multiple wells throughout the site of interest. Resolving the k distribution over an entire aquifer can require dozens or hundreds of wells and the accuracy of any k measurements may be compromised by poor well construction and experimental design [*Illman et al.,* 2007]. Extracting cores from the formation for laboratory analysis typically yields more accurate measures of k-variation throughout the aquifer. However, this approach is costly, time-consuming and provides no information on aquifer properties beyond the narrow volume from which the core were extracted, thus leading to biased sampling of the aquifer.

An alternative approach involves estimating k from the geometry of the porous medium. Pore geometries used to estimate k in consolidated materials include the pore-volume-normalized surface area [e.g. *Carman,* 1939] and the pore size distribution [e.g. *Purcell,* 1949]. *Katz and Thompson* [1986] developed a k model based on percolation theory that has been shown to accurately predict k for sandstones. The Katz and Thompson (KT) model predicts k using the characteristic hydraulic length scale of the pore space (l_c) and the intrinsic electrical formation factor (F), i.e., the true formation factor in the limit where surface conduction effects are negligible. *Katz and Thompson* [1986] define l_c from mercury injection capillary pressure (MICP) data and F requires conductivity measurements made at multiple pore fluid salinities. The nature of these measurements precludes the direct application of the KT model to field studies, limiting it to laboratory studies.

Geophysical methods sensitive to the physical properties of the subsurface offer a more labor-efficient and field-scalable approach to estimating permeability. Two geophysical methods in particular, complex conductivity (CC) and nuclear magnetic resonance (NMR), have seen increasing use for indirect permeability estimation due to their sensitivity to pore geometries [e.g. *Börner et al.,* 1996; *Banavar and Schwartz,* 1987] and applicability to field problems [e.g. *Slater and Glaser,* 2003; *Knight et al.,* 2015]. The CC relaxation time is sensitive to both the pore size distribution [*Scott and Barker,* 2003] and the tortuosity [*Weller et al.,* 2010] and the NMR relaxation time is sensitive to the pore size distribution [*Godefroy et al.,* 2001]. These geophysical methods can be used to estimate the pore geometries in the KT model, and thus can be used to model *k*. However, this approach is compromised by the non-unique relationship between the geophysical parameters and the pore-properties of interest. For instance, while the CC relaxation time may be sensitive to the pore size, it is also influenced by the mineralogy and the pore fluid chemistry [*Revil,* 2013b]. Likewise, while the NMR relaxation time is proportional to pore size, the constant of proportionality is strongly affected by the mineralogy [*Keating and Knight,* 2007]. These non-unique geophysical-pore-geometry relationships represent a primary challenge in using geophysical methods to estimate pore geometries, especially in the field [*Revil et al.,* 2015; *Behroozmand et al.,* 2015].

The consequence of this uncertainty in the petrophysical relationships used to estimate pore geometry is that the uncertainty propagates through to the CC and NMR *k* models, limiting their accuracy and applicability. We are interested in developing robust *k* models based on the KT model using CC and NMR data measureable in the field that are accurate across several orders of magnitude of *k* variation and can tolerate variability in pore geometry and mineralogy. We address the following research questions: 1) Are the CC and NMR relaxation times good proxies of l_c? and

2) Can CC data be used to effectively estimate F? We hypothesize that we can develop k models based on geophysical data that compare favorably to the KT model by understanding the relationship between CC and NMR parameters and the physical parameters l_c and F. Additionally, we examine the control of mineralogy, represented by the Fe(III) content, on the geophysical-hydraulic relationships. To the best of our knowledge, this is the first time that a joint KT model has been tested using CC and NMR data simultaneously.

In this study, we characterized a set of forty-five sandstone cores with k values varying over six orders of magnitude to test the quality of k models using CC and NMR measured parameters. We examine petrophysical relationships between the geophysical data and l_c as well as between the CC data and F in order to create a foundation on which to build and test KT models that use only CC and NMR data. We assess the quality of the new models by comparing the accuracy of k-estimates against the original KT model. As these models use geophysical parameters that are measureable in the field, they could ultimately allow hydrogeophysicists to make spatially dense, high-quality k-estimates.

2. Theory:

2.1 Katz and Thompson model

The Katz and Thompson (KT) k model is defined as:

$$k = \frac{l_c^2}{cF}, \tag{1}$$

where c is a unitless scaling constant set to 226 by *Katz and Thompson* [1986]. F is the intrinsic formation factor (unitless), which is a geophysically derived parameter and is linked to the tortuosity normalized by the interconnected porosity. *Katz and Thompson* [1986] define l_c as the percolation threshold of the pore system, or the pore size at which the entire pore space becomes hydraulically interconnected (units of meters, although the measurement is typically reported in micrometers). The authors used the inflection point of the cumulative pore size distribution determined from MICP measurements, which corresponds to the modal radius of the pore-throat size distribution (R_p), as l_c. *Johnson et al.* [1986] introduced a parameter Λ (units of meters) that represented an effective surface-area-normalized pore volume, or dynamically interconnected pore size and postulated a reformulation of the KT model in which l_c was replaced by the parameter Λ , giving:

$$k = \frac{\Lambda^2}{8F}. \tag{2}$$

Banavar and Johnson [1987] showed that Λ could be calculated from MICP data using $\Lambda \approx aR_p$. To derive a (unitless), *Banavar and Johnson* [1987] model the pore space in terms of a broad distribution of local hydraulic conductances associated with cylindrical pores. First they set the length of the pores constant and determine the percolation threshold associated with a broad distribution of pore sizes, giving a=0.51. They next consider a distribution of cylindrical pore diameters, where the length of the pores equals their diameter, to determine the percolation threshold, giving a=0.34. We assume a mixture of these types of pores are present in our samples and use an average value $a = 0.43$. *Revil et al.* [2014] used an alternative approach where they derived a scaling constant a=0.19 making equations (1) and (2) equivalent (their section 2.3); we assess how well this approach works for our data.

2.2 Complex conductivity

The complex conductivity measurement is sensitive to the reversible storage of charge in the pore space subjected to an alternating external electrical field. Ions adsorbed to the grain-mineral interface in the Stern layer lack the mobility of ions in the pore space and cannot freely migrate with an external electrical field, i.e. an injected electrical current. This creates zones of charge accumulation at the mineral-grain interface resulting in capacitive polarization of the electrical double layer surrounding the mineral grains (Stern layer polarization, see *Leroy et al.* [2008]). When the injected current takes the form of a sinusoid, the resulting waveform is a phase-delayed sinusoid with a phase lag that quantifies the extent of the capacitive polarization in the pore space. The phase lag can be used to decompose the measured complex conductivity (σ^*) into real (σ') and imaginary (σ'') components that represent electromigration and reversible storage of charge, or polarization, in the pore space, respectively [*Vinegar and Waxman*, 1984]:

$$\sigma^* = \sigma(f)' + i\sigma(f)'' \tag{3}$$

$$\sigma' = \frac{1}{F}\sigma_f + \sigma_s'. \tag{4}$$

Here, $i=\sqrt{-1}$, f is the frequency (in Hz), σ_f is the pore fluid conductivity, a function of fluid chemistry, and σ_s' is the surface conductivity which accounts for electromigration along pore surfaces. All electrical conductivity measurements in this study are in units of S m^{-1} unless otherwise stated. Complex conductivity typically refers to measurements conducted at a single frequency, while measurements performed across a range of frequencies are referred to as spectral induced polarization measurements. For the sake of simplicity, we will refer to both single and multi-frequency conductivity measurements as complex conductivity.

149 The intrinsic formation factor (hereafter referred to as F) represents the porosity
150 interconnected by electrical field lines [*Revil et al.*, 2015], which is closely related to the porosity
151 interconnected by hydraulic flow lines [*Katz and Thompson,* 1986; *Bernabe and Revil,* 1995]. F
152 was originally defined by *Archie* [1942] as the proportionality constant between σ_f and the bulk
153 DC conductivity for brine-saturated sandstones. This neglects the effect of surface conductivity,
154 and in systems where the effects of surface conduction cannot be ignored (e.g. clay-rich
155 sandstones), the approach of *Archie* [1942] produces an apparent formation factor, which
156 underestimates the true F of the system [*Weller et al.*, 2013]. Since it is not possible to separate σ_s'
157 and σ_f from σ', F can only be estimated by fitting the slope of equation (4) measured at multiple
158 pore-fluid salinities, hence the term multi-salinity formation factor. Alternatively, F can be
159 approximated by a single conductivity measurement at high pore-fluid conductivity where
160 $F^{-1}\sigma_f \gg \sigma_s'$ and Archie's Law becomes approximately true. Such a limit may be difficult to reach
161 in clay-rich sandstones with very high σ_s'. Regardless of which approach is used, neither method
162 can be used to extract F in the field, where the influence of σ_s' cannot be neglected.

163 *Börner et al.* [1996] proposed a method of estimating F using CC measurements at a single
164 fluid conductivity. The CC estimated formation factor, F_{CC}, uses $\sigma_s'=\sigma''/l$, where l is the ratio of
165 strength of electrical polarization and surface electrical conduction in the pore space, which in turn
166 yields:

$$F_{CC}=\frac{\sigma_f}{\sigma'-\sigma''/l}. \tag{5}$$

167 *Weller et al.* [2013] found that values of F_{CC} determined using $l = 0.042$ (unitless) compared
168 favorably with F for data collected at 1 Hz with $\sigma_f \approx 100$ mS m^{-1} across a wide range of

sandstones. *Revil* [2013a] derived an equivalent scaling parameter relating σ_s' and σ'' based on the mobility of ions in the Stern Layer and the bulk pore fluid (their equation 87) and *Revil et al.* [2015] used this result to calculate F_{CC} for their *k* models where only the apparent formation factor was available. By employing F_{CC} from equation (5) to estimate F in equation (2), we can avoid the necessity of multi-salinity measurements. This potentially allows the model to be applied directly in the field, where an estimate of σ_f exists.

The phase spectrum can be represented by a CC relaxation time, τ (units of seconds), or a distribution of relaxation times, which are a measure of the time required for polarized ions to return to equilibrium when the external electrical field is terminated. *Revil et al.* [2015] proposed an approach to determine a characteristic relaxation time, τ_p, from the spectrum. The frequency of the local peak for the phase spectrum is selected where such a local maxima in σ'' exists, following the approach of *Scott and Barker* [2003]. Otherwise, for cores with a plateau in the spectrum they chose the lowest frequency at the low-frequency end of the plateau. The characteristic τ_p is then calculated as:

$$\tau_p = \frac{1}{2\pi f_p}, \tag{6}$$

where f_p is the characteristic frequency chosen from the approach of *Revil et al.* [2015]. This frequency is assumed to be correlated to the largest length scale in the pore space that controls electrical polarization and, by analogy, fluid flow [*Kruschwitz et al.,* 2010]. Alternative methods of calculating τ from phenomenological models include using the Cole-Cole model to extract a single CC relaxation time [e.g. *Binley et al.,* 2005] (note that Cole-Cole time constants are often referred to as C-C time constants, which should not be confused with the CC relaxation time we

derive) or fitting a distribution of τ values to the spectrum using either the Debye decomposition [*Nordsiek and Weller,* 2008] or the Warburg model [*Revil et al.,* 2014]. We eschew these approaches in favor of the simpler approach of *Revil et al.* [2015] as the Cole-Cole model, which assumes a logarithmically symmetric peak in the phase spectrum, does not apply to much of our data and *Niu and Revil* [2016] demonstrate that there is still considerable uncertainty in fitting a Debye or Warburg model to CC spectra.

Scott and Barker [2003] found that the inverse of f_p was linked to the pore throat size from MICP for a number of Permo-Triassic sandstone cores. *Binley et al.* [2005], also working with Permo-Triassic sandstones, demonstrated a strong power-law relationship between the CC relaxation time and permeability. *Revil* [2013b] developed a mechanistic model to determine the pore geometry by substituting Λ for the colloid radius in the model of *Schwarz* [1962], giving:

$$\tau_p = \frac{\Lambda^2}{2D_{(+)}^S}, \tag{7}$$

where $D_{(+)}^S$ is the ionic diffusivity of the Stern Layer (units of $m^2\ s^{-1}$). $D_{(+)}^S$ is controlled both by the pore fluid chemistry and the mineralogy [*Revil,* 2013a] meaning it is a primary source of uncertainty in this CC petrophysical model; *Revil* [2013b] derived $D_{(+)}^S = 3.8\text{x}10^{-12}\ m^2\ s^{-1}$ for clay-bearing sandstones saturated with a sodium chloride brine at 25 °C and a value of $D_{(+)}^S = 1.3\text{x}10^{-9}\ m^2\ s^{-1}$ for clay-free sandstones. The value of $D_{(+)}^S$ for clayey sands was calculated from values of the ionic mobility of the Stern Layer *Revil* [2012] derived based on measurements from *Vinegar and Waxman* [1984].

2.3 Nuclear magnetic resonance

In hydrogeophysics, the NMR phenomenon arises as a result of the alignment of the nuclear spins of hydrogen protons in water with a static magnetic field, which produces a bulk magnetization $\boldsymbol{M}$. The transverse component of $\boldsymbol{M}$ can be detected by tipping the spins out of alignment with the static magnetic field using a series of oscillating magnetic field pulses, called the CPMG (Carr-Purcell-Meiboom-Gill) pulse sequence, and measuring a voltage induced by their return to equilibrium during this pulse sequence. The CPMG pulse sequence consists of a pulse that tips the spins 90° from their alignment with the static field followed by a series of 180° pulses separated by an interval called the echo time; the 180° pulses serve to realign spins that have drifted out of phase due to magnetic field inhomogeneities. The resulting measured signal is a superposition of multiple exponential decays. The initial amplitude of the signal is proportional to the number of protons, which corresponds to the total volume of water, and, in water-saturated porous media, the distribution of decay times is related to the pore-size distribution and the mineralogy of the measured volume.

In sandstones, relaxation typically occurs within the fast diffusion regime [*Brownstein and Tarr*, 1979; *Kleinberg and Horsfield*, 1990] and can be modeled as the sum of exponential decays where each exponential amplitude and transverse relaxation time corresponds to a single pore environment. When inverted, the NMR signal is represented by the plot of the amplitudes versus the associated transverse relaxation times or T_2-distribution. A characteristic relaxation time value, such as the mean-log relaxation time (T_{2ml}) or the relaxation time associated with the peak of the distribution (T_{2p}), is used to represent the T_2-distribution. For simplicity, we refer to the characteristic relaxation time as T_2 (units of seconds).

T_2 is the sum of three relaxation processing acting in parallel:

$$T_2^{-1}=T_{2B}^{-1}+T_{2S}^{-1}+T_{2D}^{-1}, \quad (8)$$

where T_{2B} is the bulk relaxation time associated with the pore fluid, T_{2S} is surface relaxation time, and T_{2D} is the diffusion relaxation time. In sandstones, bulk fluid relaxation is typically considered negligible since $T_{2S} \ll T_{2B}$ [*Arns et al.,* 2005], an assumption that can be checked by comparing T_2 with T_{2B} determined from a measurement on the pore fluid. Diffusion relaxation results from the dephasing of the spins in an inhomogeneous magnetic field, which is minimized by making measurements using the CPMG pulse sequence with short echo times, and is often assumed to be negligible. The assumption that T_{2D} is negligible can be tested by collecting measurements at multiple echo times; if T_2 does not change as a function of echo time then this assumption is correct [*Kleinberg and Horsfield*, 1990]. Assuming bulk and diffusion relaxation are negligible, equation (8) can be simplified to $T_2^{-1} \approx T_{2S}^{-1}$.

T_{2S} is a function of the pore size and is represented by [*Brownstein and Tarr,* 1979]:

$$T_2^{-1} \approx T_{2S}^{-1} = \alpha \rho_2 R_p^{-1} \quad (9)$$

where ρ_2 (in μm s^{-1}) is the surface relaxivity and α is a unitless shape factor of the pore space. The value of ρ_2 is controlled by the density and distribution of unpaired electrons at the pore surface where the spin coupling between the electrons and the hydrogen protons accelerates relaxation [*Godefroy et al.,* 2001]. These unpaired electrons are associated with paramagnetic impurities, for example Fe(III) in common iron oxides such as hematite or goethite [*Keating and Knight,* 2007]. Equation (9) is the basis for using NMR measurements to estimate permeability in porous media [*Banavar and Schwartz,* 1987].

Using the approach of *Banavar and Johnson* [1987], we extend equation (9) to include Λ:

$$T_2^{-1}=\rho_{2eff}\Lambda^{-1} \quad (10)$$

where $\rho_{2eff} = \alpha a \rho_2$ is an effective ρ_2 used to account for the unitless factors that relate Λ and R_p. *Marschall et al.* [1995] proposed a rigorous method for deriving ρ_2 that provides the best fit between the T_2 and MICP distributions and found that ρ_2 for sandstones ranges from 6.4 to 25 μm s^{-1}, equivalent to a ρ_{2eff} range of 2.8 to 11 μm s^{-1}. Using similar approaches, other authors have calculated values for ρ_2 in the same range [*Morriss et al.*, 1993; *Straley et al.*, 1994].

2.4 Petrophysical permeability models

By substituting Λ approximated from equations (7) and (10) and the value of F_{CC} for F from equation (5) into equation (2), we derive two k models:

$$k=\frac{D_{(+)}^{S}\tau_p}{4F_{CC}}, \quad (11)$$

$$k=\frac{\left(\rho_{2eff}T_2\right)^2}{8F_{CC}}. \quad (12)$$

Equation (11) is the same model proposed by *Revil et al.* [2015], although the authors used the intrinsic F, and equation (12) is structurally similar to an empirical model proposed by *Dunn et al.* [1999], which uses NMR relaxation times and the intrinsic F to estimate k in sandstones. Our models in equation (11) and (12) are distinct from their predecessors as they only employ geophysical parameters measureable in the field, although they use a single fitting factor each ($D_{(+)}^{S}$ in equation (11) and ρ_{2eff} in equation (12)).

3. Materials and methods

Forty-five sandstone cores from fifteen different formations were used in this study. The formation and associated sample names are listed in Table 1. Cores from the Clashach, Doddington, and Sherwood sandstone formations were sourced from the United Kingdom; cores from the Arizona Chocolate, Berea, Island Rust, Pennsylvania Blue and Tennessee sandstone formations were sourced from the United States; cores from the Bentheimer, Cottaer, Elb, Gravenhorster and Obernkirchener formations were sourced from Germany. The sandstones are primarily composed of quartz and feldspar with variable binding phases including kaolinite, iron oxide and carbonate. Detailed lithological descriptions of the Arizona Chocolate, Berea, Coconino, Island Rust and Tennessee sandstones can be found in *Baker* [2001] and descriptions of the Bentheimer and Cottaer sandstones can be found in *Kruschwitz* [2008]. *Binley et al.* [2005] describe the physical characteristics of the Sherwood cores HEC18-7, VEC15-5, and VEG2RI-2 while *Mejus* [2015] describes cores SB1-SB7 from the St. Bees formation of the Sherwood group. Some data presented in this study have recently appeared in *Keery et al.* [2012], *Revil et al.* [2015], and *Weller et al.* [2015]. With the exception of the Clashach, Pennsylvania Blue, and Sherwood cores, replicate cores were subsampled from similar locations in the larger drilled cores for each formation and used to quantify the variability in physical and geophysical properties within a small volume of the formation. Only a single core was available from each of the Clashach and Pennsylvania Blue formations; the Sherwood cores were subsampled from different sections of larger drilled cores.

Gas-k data were collected for each core while pore throat size distributions from MICP were measured on material from each formation and each of the Sherwood cores. MICP data for the Arizona Chocolate, Berea, Coconino, Island Rust and Tennessee formations are from *Baker*

288 [2001] and for the Bentheimer, Cottaer, Elb, Gravenhorster, Obernkirchener, and Pennsylvania
289 Blue formations are from *Kruschwitz et al.* [2010]. MICP and *k* data for the Sherwood cores
290 HEC18-7, VEC15-5 and VEG2RI-2 are from *Binley et al.* [2005] and *k* data for SB1-SB7 are from
291 *Mejus* [2015]. Permeability values have previously been published for cores AC2, AC4, B4, Be1,
292 C33, Clash1, Co7, E3, G4, IR01, IR02, O5, PB5, T2, and T5 [*Baker,* 2001; *Kruschwitz,* 2008;
293 *Kruschwitz et al.,* 2010; *Binley et al.,* 2005; *Mejus* 2015), however, we remeasured *k* for these
294 cores to better resolve values of k <0.01 mD. We used a Core Laboratories CMS-300 N_2 gas
295 permeameter designed for measuring sub-μD *k* values and applied a Klinkenberg correction
296 [*Klinkenberg,* 1941]. The new *k* values closely matched the original *k* values except in the range
297 of k<0.01 mD where the newer measurements were more accurate. MICP data for SB1-SB7 as
298 well as for the Doddington cores were acquired from a Micromeritics Autopore V. All calculations
299 were performed using SI units, however, *k* values are reported in milliDarcies rather than m^2 for
300 consistency with the literature.

301 Prior to the geophysical measurements, the cores were oven dried overnight at 200ºC
302 (longer if the cores started saturated) then vacuum saturated with a sodium chloride brine. CC data
303 were collected using the ZEL-SIP04-V02 with frequencies ranging from 2 mHz-45 kHz using a
304 sample holder arrangement as shown in *Binley et al.* [2005]; a detailed description of the
305 instrumentation can be found in *Zimmermann et al.* [2008]. CC measurements for most cores were
306 made with brine concentrations ranging from 0.01 M to 1 M in order to extract F and σ_s'. For cores
307 AC2, B10, Co8, D3, and VEC15-5 low salinity (0.01 M) CC data were not available. For the
308 Doddington formation and the core Co4, the high salinity (1M) CC data were not available and we
309 were unable to calculate F for these cores. While these cores are not included in the CC
310 petrophysical analysis or permeability models, they are used to determine ρ_{2eff}. F_{CC} was calculated

using equation (5) at a NaCl concentration of 0.01 M and a frequency of 1 Hz. To select f_p, we followed the approach of *Revil et al.* [2015]. If a distinct peak was visible in the CC spectra, the frequency of the peak was chosen as f_p. In the case where no peak was discernable, we selected the low-frequency inflection point where the spectra begins to flatten out (see *Revil et al.* [2015], their Figure 3).

NMR data were collected using a Magritek 2.0 MHz Rock Core Analyzer on cores saturated with a 0.01 M NaCl brine. Data were collected using the CPMG pulse sequence with echo times of 200, 400, 800 and 1600 μs, such that the effect of diffusion relaxation could be assessed; the number of echoes was selected such that the data record was 10 s long with a recovery time of 10 s and the data were stacked until a signal-to-noise ratio of at least 200 was attained. The T_2 decay curves were inverted to yield the T_2-distribution using a non-negative least-squares algorithm with Tikhonov regularization [*Whittall et al.,* 1991]. The regularization parameter chosen was the largest regularization parameter that produced the lowest normalized root mean squared error, as described in *Costabel and Yaramanci* [2013]. We use T_{2p} as a proxy for the peak of the MICP pore throat size distribution, and therefore Λ, in our petrophysical models.

To account for differences in the geophysical measurements in the cores due to the presence of paramagnetic impurities, we measured the iron content using material from the Arizona Chocolate, Berea, Cottaer, Coconino, Doddington, Pennsylvania Blue and Tennessee formations as well as separate material from cores SB1-SB7 of the Sherwood group. To measure the iron (specifically Fe(III)) content, pieces of the sandstone were ground up and then digested in acid (6 M HCl) for one week to dissolve iron from the surface of the grains. Fe(III) content (mg(Fe)/g(sample) was then measured spectrophotometrically using the ferrozine method [*Stookey,* 1970].

334 The ionic diffusivity of the Stern Layer $\left(D_{(+)}^{S}\right)$ and the effective NMR surface relaxivity
335 $\left(\rho_{2eff}\right)$ were derived from the geophysical-hydraulic relationships in equations (7) and (10) using
336 linear regression. For our *k* models, we first test the KT model given in equation (2) using Λ (from
337 MICP data) and *F* (from multi-salinity electrical conductivity measurements), in order to
338 determine the best possible estimate of *k* that can be derived for these cores. We calculate Λ from
339 our MICP data using a value of *a*=0.43 [*Banavar and Johnson et al.*, 1987]. In the CC-*k* model
340 from equation (11), *k* is determined using $\Lambda^2 = 2D_{(+)}^{S}\tau_p$ and $F = F_{CC}$. In the NMR-CC-*k* model
341 from equation (12), *k* is calculated using $\Lambda = \rho_{2eff}T_{2p}$ and $F = F_{CC}$. For all *k* models, we use the
342 normalized root mean square error (NRMSE) between measured and modeled *k* in order to
343 compare the KT and geophysical-*k* models:

$$NRMSE = \frac{1}{y_{rng}}\sqrt{\sum \frac{\left(\hat{y}_t - y\right)^2}{n}}. \tag{13}$$

344 $\hat{y}_t$ is the predicted value, *y* is the true measured value, y_{rng} is the range of measured values, and *n*
345 is the number of predictors. All NRMSE calculations are performed in log-space.

346 **4. Results**

347 Table 1 summarizes measured values for Λ (from MICP measurements), *k* and Fe(III)
348 content. Λ ranges from 0.02 μm for the Pennsylvania Blue core to 10.53 μm for the Elb cores.
349 Permeability spans over six orders of magnitude from 9.34×10^{-4} mD for PB5 to 4.62×10^{3} mD for
350 E7. Measured Fe(III) content varies from 0.33 mg g^{-1} in the Berea formation to 16.12 mg g^{-1} for
351 Sherwood core SB6.

Pore size distributions from MICP, NMR T_2-distributions and CC spectra for D1 (Doddington formation), SB4 (Sherwood group), G2 (Gravenhorster formation), and PB5 (Pennsylvania Blue formation) are shown, along with the permeability values, in Figure 1. These cores are representative of the range of the physical and geophysical data collected. A similar set of plots from four additional cores are included as supporting information (Figure S1). From the MICP data, D1 has a high porosity dominated by large pores, consistent with the high *k* value. SB4 has a smaller porosity with smaller pores and a lower measured *k*. G2 has a similar pore-throat size distribution to SB4 and the cores have similar *k* values. Lastly, PB5 has the lowest porosity in Figure 1, very small pores and, correspondingly, has the lowest measured *k*.

For the CC data, we expect f_p to increase with decreasing pore size. In the σ'' spectrum for D1, f_p is very low and the σ'' spectrum is low amplitude, consistent with the low surface area of the sample [*Slater and Glaser*, 2003]. The σ'' spectrum for SB4 behaves very differently from the rest of the cores in Figure 1. While f_p is located at intermediate frequencies, consistent with the medium-sized pores seen in the MICP distribution, the σ'' spectrum shows a very distinct, high-amplitude peak. The σ'' spectrum for G2 shows a higher f_p value than is seen in D1, consistent with the smaller pores in this sample, and a higher σ'' amplitude, likely reflecting the increased surface area of the sample. However, f_p in G2 is almost an order of magnitude smaller than for SB4, which we would not expect as the peak pore sizes for the two cores are nearly identical. PB5 has a low f_p and the σ'' spectrum is flat with a low amplitude, contrasting with our expectation that a sample with very tight pores should have a high f_p. This anomalous f_p is also seen in the low-permeability Arizona Chocolate and Tennessee cores. These results are consistent with the results given in *Kruschwitz et al.* [2010] from measurements made on a subset of these cores.

NMR T_2 distributions should correlate with the MICP pore throat size distributions. This is the case for D1; the T_2 distribution has a large total signal amplitude and the distribution is centered on long T_2 values. SB4 has a lower signal amplitude centered on medium T_2 values, however the T_2 distribution is very broad, likely a result of the higher Fe(III) concentration in SB4 than in G2; *Keating and Knight* [2007] observed a similar broadening of the T_2-distribution with the addition of Fe(III) minerals to sand packs. The T_2 distribution for G2 has a similar signal amplitude as SB4, centered on medium T_2 values as well, but the distribution is more concentrated in a single peak. PB5, the tightest core, has the lowest total NMR signal amplitude and the distribution is centered on the shortest T_2 values.

4.1 Hydraulic length scale relationships

Figure 2A shows the linear regressions between τ_p and $\Lambda^2/2$ used to derive $D^S_{(+)}$ from equation (7); Figure 2B shows the linear regression between T^1_{2p} and Λ^{-1} used to derive ρ_{2eff} from equation (10). The CC and NMR parameters used in these figures are given in Table 2. For each plot, the size of the data point represents the log(k) value for that core. The coefficients of determination (R^2) for each of the linear regressions are shown on the plot. The errors given for the fitting coefficients determined from the slopes of the linear regressions are the 95% confidence intervals. As highlighted in Figure 1, the Sherwood cores show distinct CC and NMR behavior; for this reason we use square data points to distinguish these cores.

The slope of the line fit to $\Lambda^2/2$ versus τ_p (Figure 2A) gives $D^S_{(+)} = (2.9\pm2.0)\text{x}10^{-12}$ m^2 s^{-1}. The 95% confidence interval includes the value of $D^S_{(+)}$ *Revil* [2013b] derived for clay-bearing sands ($D^S_{(+)} = 3.8\text{x}10^{-12}$ m^2 s^{-1}). Overall, the quality of the fit is poor, with an R^2 value of 0.39, an NRMSE of 0.20 and a large error on the value of the slope (Figure 2A). However, the Sherwood

cores follow the expected relationship from equation (7), supporting the findings of *Binley et al.* [2005]; if the Sherwood cores were removed no correlation between $\Lambda^2/2$ and τ_p in the remaining cores would be observed. Cores from the Tennessee (T), Arizona Chocolate (AC) and Pennsylvania Blue (PB) formations (given by filled circles in Figure 2A) display anomalous behavior that was also observed in *Kruschwitz et al.* [2010] and *Revil et al.* [2015]. *Kruschwitz et al.* [2010] reasoned that the pore size for these cores was not the dominant length scale controlling polarization. These cores therefore cannot be modeled using equation (7) and have been excluded from our fit.

In Figure 2B, the slope of the fit to Λ versus T_{2p} gives $\rho_{2eff} = 25.4 \pm 6.6$ μm s^{-1}. The quality of the fit is much better than the relationship for the CC data with an R^2 of 0.696 and an NRMSE of 0.16. However, the value determined for ρ_{2eff} is higher than the maximum values derived from *Marschall et al.* [1995]. As with the CC results in Figure 2A, the Sherwood cores show distinct behavior and have consistently shorter T_{2p} values associated with similar Λ values than the cores from other formations.

Figure 3 shows the relationship between F, determined from multi-salinity measurements, and F_{CC} calculated from σ' and σ'' for measurements made on cores saturated with a 10mM NaCl brine ($\sigma_f \approx 100$ mS m^{-1}) using equation (5). The values used in this figure are given in Table 2. The solid line is the 1:1 line. The NRMSE value for the entire dataset is 0.23. For most cores, $F_{CC} \sim F$, consistent with the results of *Weller et al.* [2013]; however, F is underestimated for many of the cores from the Sherwood group which display high-amplitude σ'' spectra (e.g. SB4 in Figure 1), as well as for cores with very low k.

4.2 Katz and Thompson model

418 The plot of the KT-modeled *k* versus the measured *k* (Figure 4) shows that the KT model
419 provides accurate predictions over a wide range of measured *k*. All but one of the cores fall within
420 the +/- one order of magnitude bounds and the overall fit has a NRMSE value of 0.074, calculated
421 using the *k* values determined with the KT-model and the measured *k* values. The KT model will
422 be the benchmark with which we compare the geophysical-*k* models.

423 **4.3 Petrophysical permeability models**

424 The CC-*k* model from equation (11) and the NMR-CC-*k* model from equation (12) are
425 shown in Figure 5. The models use $D^{S}_{(+)}$ and ρ_{2eff} determined from the plots in Figures 2A and 2B,
426 respectively. Overall, CC estimates of *k* are quite poor (NRMSE=0.23). Predicted *k* for many cores
427 shows little variation while measured *k* ranges over approximately four orders magnitude, resulting
428 in discrepancies between modeled- and measured-*k* values greater than one order of magnitude
429 (indicated by the dashed lines in Figure 5). Data excluded from the CC-hydraulic length-scale
430 relationship (Figure 2A) were not included in the calculation of the NRMSE for the CC-*k* model
431 in Figure 5A. In contrast, the NMR-CC-*k* model provides good estimates of *k* (NRMSE=0.13),
432 which are, with a few exceptions, consistently within the one order of magnitude bounds. Based
433 on the NRMSE values, the NMR-CC-*k* model provides superior *k* estimates over the CC-*k* model.
434 The behavior of the Sherwood cores again deviates from the behavior of the rest of the cores; the
435 NMR-CC-*k* model consistently underestimates *k* for these cores.

436 **4.4 Iron Content Data**

437 The measured Fe(III) content is plotted against $\Lambda/T_{2p}\,(=\rho_{2eff})$ in Figure 6 and shows that
438 ρ_{2eff} ranges from 4.8 to 258 μm s^{-1} for the cores in this study. These values are larger than those
439 typically associated with sandstone cores but are within the range that *Keating and Knight* [2007]

measured for sands ($\rho_2 = 0.31$) and Fe(III)-coated sands (maximum of $\rho_2 = 292$ μm for a magnetite-coated sand). The values from *Keating and Knight* were calculated using the pore volume-normalized surface area in place of $\alpha(R_p)^{-1}$ in equation (9), which would give lower ρ_2 values than would be derived with our approach. Figure 6 shows that although in general, the Sherwood cores (open squares) show a higher Fe(III) content and a higher value of Λ/T_{2p} than was measured for the other sandstones, there is no clear trend between Λ/T_{2p} and Fe(III) content. Cores from the Arizona Chocolate and Pennsylvania Blue formations also have high Fe(III) content but a low Λ/T_{2p} value.

5. Discussion

Our results demonstrate that the KT model, using Λ from MICP measurements and F derived from multi-salinity conductivity measurements (Figure 4) reliably predicts k for sandstone cores in the laboratory (NRMSE=0.074) over six orders of k-variation. Furthermore, they suggest that geophysical methods sensitive to these pore geometries can be used in the KT model to indirectly estimate k. We first examine the relationship between our geophysical relaxation times (CC and NMR) and Λ, as well as the relationship between F_{CC} and F. We then compare the predictive power of k models using geophysical parameters with the KT model. Lastly, we discuss sources of error in the data and the limitations of the models, as well as the applicability of these findings to future laboratory and field datasets.

Figure 2 shows that the NMR data provide reasonable predictions of Λ for the entire dataset (R^2=0.69) and superior predictions compared to those from the CC data (R^2=0.39). Figure 3 shows that F_{CC} is an effective proxy for F (NRMSE of 0.23) providing a measurement of the effective

462 porosity. Based on the results in Figure 2, we produced an NMR-CC-*k* model (equation (12);
463 Figure 5B) that gives superior *k* estimates over the CC-*k* model (equation (11); Figure 5A), with
464 NRMSE values of 0.13 and 0.23, respectively. The importance of Λ in the KT model is highlighted
465 here, as the difference in the *k* estimates reflects differences between the NMR and CC estimates
466 of Λ. Although the *k*-estimates from the NMR-CC-*k* model are inferior to those of the KT model,
467 the NMR-CC-*k* model parameters are directly measureable using borehole instrumentation.
468 Applying equation (12) in situ would require an NMR T_2 measurement, a complex conductivity
469 measurement at 1 Hz, a measurement of the pore fluid conductivity, and an estimate of ρ_{2eff}.

470 A potential source of error in the CC-*k* and NMR-CC-*k* models is the choice of *a* in the
471 calculation of Λ; no rigorous derivation of the parameter *a* exists and we assumed *a*=0.43 as a
472 means of averaging the two pore environments modeled by *Banavar and Johnson* [1987]. We
473 examined the relationship between *a* and the NRMSE of the KT model (supporting information,
474 Figure S2) and found that the NRMSE reached a minimum at *a*=0.45. This suggests that the value
475 of *a* we use is more appropriate for our data than the value *Revil et al.* [2014] proposed (*a*=0.19)
476 to make equations (1) and (2) equivalent.

477 We observe behavior in the CC and the NMR data collected on the Sherwood cores that is
478 inconsistent with the other cores. For the CC data, the Sherwood cores display the expected linear
479 relationship between τ_p and $\Lambda^2/2$ (Figure 2A) while the remaining cores do not. However, F_{CC} is
480 consistently a poor predictor of *F* for the Sherwood cores when compared with the entire dataset
481 (Figure 3). *Mejus* [2015] observed related anomalous behavior for cores SB1-SB7. Contemporary
482 CC theory cannot predict the behavior of these cores based on their pore geometry and we instead
483 believe that the mineral properties of these cores are the cause of their behavior. For the NMR

484 data the Sherwood cores consistently have shorter T_{2p} values compared to the rest of the cores
485 (Figure 2B). We again attribute the behavior of the Sherwood cores to the mineralogy of the cores.

486 A major limitation of our modeling approach arises from the uncertainty in the choice of
487 the fitting parameters $D^S_{(+)}$ and ρ_{2eff}. The values of $D^S_{(+)}$ and ρ_{2eff} are controlled by mineralogical
488 properties and using a single fitting parameter for a set of cores with varying mineralogies
489 compromises our ability to effectively estimate Λ and ultimately limits the accuracy of CC-*k* and
490 NMR-CC-*k* models. While our derived CC fitting parameter $D^S_{(+)}$ is consistent with the value given
491 by *Revil* [2013b] for clay-bearing sandstones, the wide confidence intervals associated with the
492 parameter (+/-2.0x10^{-12} m^2 s^{-1}) suggest that a range of $D^S_{(+)}$ may be necessary to model the CC
493 response in sandstones. Additionally, we do not account for the potential effect of polarization in
494 the diffuse layer in our calculation of $D^S_{(+)}$, as described in *Niu and Revil* [2016], as our approach
495 does not allow us to separate the effects of $D^S_{(+)}$ and the correction coefficient the authors define
496 (their equation 26). Similarly, we use a single value for ρ_{2eff} even though the parameter can span
497 multiple orders of magnitude (Figure 6) depending on factors including the concentration, spatial
498 distribution and mineralogical form of paramagnetic impurities such as Fe(III) [*Foley et al.*, 1996;
499 *Keating and Knight*, 2007, 2012]. While this approach produces reasonable estimates of *k* for our
500 dataset (Figure 5B), the variability of ρ_{2eff} is a major source of uncertainty in the NMR-CC-*k*
501 model. Figure 2B suggests that using two values of ρ_{2eff} (one for the Sherwood cores, one for the
502 remaining cores) may be appropriate for the describing this dataset, as the Sherwood cores
503 consistently display elevated T_{2p}^{-1} values. In Figure 6, we attempted to show that high Fe(III)
504 content in the Sherwood cores could explain the elevated T_{2p}^{-1} values and justify the use of a
505 separate ρ_{2eff} for these cores; however, Figure 6 also shows high Fe(III) content for AC and PB,

cores that do not display elevated T_{2p}^{-1} values in Figure 2B, suggesting that Fe(III) content alone cannot be used to justify using an additional ρ_{2eff} parameter. Accounting for the uncertainty in *k* models resulting from the choice of $D_{(+)}^{S}$ and ρ_{2eff} is essential before these *k* models can be applied in the field and future work should focus on non-sandstone materials (e.g. carbonates [e.g. *Halisch et al.*, 2014; *Schoenfelder et al.*, 2008], unconsolidated sediments [e.g. *Weller et al.*, 2015; *Dlugosch et al.*, 2013]) with a range of mineralogies.

Alternative models of permeability prediction using CC or NMR data have been proposed. *Revil and Florsch* [2010] proposed a *k* model based on grain polarization that related *k* to *F* and *σ″*. *Weller et al.* [2015] derives structurally similar empirical *k* models for a dataset spanning 56 sandstones. Additionally, numerous models exist that model *k* from the proportions of the pore space thought to support fluid flow (i.e. the free fluid index, see *Timur*, [1969]). We have found that the CC-NMR-KT model provides superior *k*-estimates for our cores than these alternative models, especially when estimating *F* with CC data. These models suggest, however, that additional information contained in our geophysical data may be useful for improving future *k* models.

Future work must also determine how well our CC-*k* and NMR-CC-*k* models, which were developed in controlled laboratory conditions, can be applied to field studies. The support volume of the measurement varies depending on the both the method (CC or NMR) and instrument (surface versus borehole) used; field-scale heterogeneities (e.g. preferential flow paths) included within different support volumes will challenge our ability to upscale our *k* models. Furthermore, field measurements have lower signal-to-noise ratios than laboratory measurements, which will reduce the accuracy of *k* models. A critical next step is to assess the accuracy and scalability of the

528 *k* models at a site where laboratory and field CC and NMR data can be compared to direct
529 measurements of *k*.

530

531 **6. Conclusions**

532 We derived relationships between geophysical parameters and the hydraulic parameters
533 of the *Katz and Thompson* [1986] permeability model (KT model) for sandstone cores. The NMR
534 data effectively model the pore size parameter measured from MICP measurements in the KT
535 model while CC measurements can be used to estimate the intrinsic formation factor, a
536 measurement of the effective porosity. Using the hydraulic parameters estimated from geophysical
537 measurements, we tested a robust, joint NMR-CC-permeability model capable of accurately
538 estimating permeability over six orders of magnitude. This model represents an improvement over
539 previous KT models based on CC or NMR data in that it only uses geophysical parameters
540 potentially measureable in the field. The Sherwood cores display distinct behavior and their NMR
541 behavior cannot be explained in terms of Fe(III) content alone. This behavior illustrates the
542 uncertainty introduced into the *k* model as a result of the surface relaxivity fitting parameter, which
543 is strongly controlled by mineralogy. While this work demonstrates that an improved *k*-model can
544 be obtained from combining NMR and CC measurements, future work is necessary to understand
545 the influence of mineralogy on the surface relaxivity as well the applicability of the model in the
546 field.

547

548 **Acknowledgements**

We thank Mejus Lakam and Samantha France (Lancaster University, UK) as well as Ryan McDonald (Rutgers University-Newark, USA) for assistance with the CC data acquisition, Judy Robinson, and Tonian Robinson (Rutgers University-Newark, USA) for assistance with the iron content analysis, as well as Manika Prasad, Elshan Aliyev and Joe Chen (Colorado School of Mines, USA) for assistance in collecting much of the permeability data. David Lesmes (Department of Energy, USA), Sabine Kruschwitz (BAM, Germany), Quentin Fischer (University of Leeds, UK) and Andy Butcher (British Geological Survey, UK), contributed data and materials for the research. Data used specifically in this study are given in Tables 1 and 2 and any data acquired by the authors will be available upon request from the corresponding author one year after publication; sources for any data previously published are given in the Materials and Methods section. Lastly, we thank André Revil, Andreas Weller, and one anonymous reviewer for their insightful comments that helped improve this manuscript. This research was based on work supported by the National Science Foundation under Grant No. 1246507.

References

Archie, G., (1942), The Electrical Resistivity Log as an Aid in Determining Some Reservoir Characteristics, Transactions of the American Institute of Mining, Metallurgical, and Petroleum Engineers, 146, 54–62, doi: 10.11159/ijmem.2012.008.

Arns, C., M. Knackstedt, and N. Martys, (2005), Cross-Property Correlations and Permeability Estimation in Sandstone, Physical Review E - Statistical, Nonlinear, and Soft Matter Physics, 72, 1–12, doi: 10.1103/PhysRevE.72.046304.

Banavar, J. and L. Schwartz, (1987), Magnetic Resonance as a Probe of Permeability in Porous Media, Physical Review Letters 58 (14), 1411–1414, doi: 10.1103/PhysRevLett.58.1411.

571 Banavar, J., and D. Johnson, (1987), Characteristic Pore Sizes and Transport in Porous Media,
572 Physical Review B, 35(13), 7283–7286, doi: 10.1103/PhysRevB.35.7283.

573 Baker, H. (2001). Prediction of capillary pressure curves using dielectric spectra, Masters Thesis,
574 Department of Geology and Geophysics, Boston College, Boston, USA.

575 Behroozmand, A., K. Keating, and E. Auken, (2015). A Review of the Principles and
576 Applications of the NMR Technique for Near-Surface Characterization. Surveys in
577 Geophysics, 36, 27–85, doi: 10.1007/s10712-014-9304-0.

578 Bernabe, Y., and A. Revil (1995), Pore-scale heterogeneity, energy dissipation and the transport
579 properties of rocks, *Geophys. Res. Lett., 22*(12), 1529–1532, doi:10.1029/95GL01418.

580 Binley, A., L. Slater, M. Fukes, and G. Cassiani, (2005), Relationship between Spectral Induced
581 Polarization and Hydraulic Properties of Saturated and Unsaturated Sandstone, Water
582 Resources Research, 41(12), W12417, doi: 10.1029/2005WR004202.

583 Brownstein, K., and C. Tarr, (1979), Importance of Classical Diffusion in NMR Studies of Water
584 in Biological Cells, Physical Review A, 19(6), 2446–2453, doi:
585 10.1103/PhysRevA.19.2446.

586 Börner, F., J. Schopper, and A. Weller, (1996), Evaluation of Transport and Storage Properties in
587 the Soil and Groundwater Zone from Induced Polarization Measurements, Geophysical
588 Prospecting, 44(5), 583–601, doi: 10.1111/j.1365-2478.1996.tb00167.x.

589 Carman, P.C., (1939), Permeability of saturated sands, soils and clays. The Journal of
590 Agricultural Science, 29, pp 262-273. doi:10.1017/S0021859600051789.

591 Costabel, S., and U. Yaramanci, (2013), Estimation of Water Retention Parameters from Nuclear
592 Magnetic Resonance Relaxation Time Distributions, Water Resources Research, 49(4),
593 2068–2079, doi: 10.1002/wrcr.20207.

594 Dlugosch, R., T. Günther, M. Müller-Petke, and U. Yaramanci (2013), Improved prediction of
595 hydraulic conductivity for coarse-grained, unconsolidated material from nuclear magnetic
596 resonance, Geophysics, *78*(4), EN55–EN64, doi:10.1190/geo2012-0187.1.Dunn, K., G.
597 Latorraca, and D. Bergman, (1999), Permeability Relation with Other Petrophysical
598 Parameters for Periodic Porous Media, Geophysics, 64(2), 470–478, doi: 10.1016/S0730-
599 725X(98)00055-1

600 Foley, I., S. Farooqui, and R. Kleinberg (1996), Effect of Paramagnetic Ions on NMR Relaxation
601 of Fluids at Solid Surfaces, Journal of Magnetic Resonance Series A, 123(1), 95–104,
602 doi:10.1006/jmra.1996.0218.

603 Godefroy, S., J. Korb, M. Fleury, and R. Bryant, (2001), Surface Nuclear Magnetic Relaxation
604 and Dynamics of Water and Oil in Macroporous Media, Physical Review E, 64(2), 021605,
605 doi: 10.1103/PhysRevE.64.021605.

606 Halisch, M., A. Weller, S. Hupfer, and M. Kassab (2014), Impedance spectroscopy on
607 carbonates, in International Symposium of the Society of Core Analysts, pp. 1–6, Avignon,
608 France.

609 Illman, W., A. Craig, and X. Liu, (2007), Practical Issues in Imaging Hydraulic Conductivity
610 through Hydraulic Tomography Practical Issues in Imaging Hydraulic Conductivity through

611 Hydraulic Tomography, Groundwater, 46(1), 120–132, doi: 10.1111/j.1745-
612 6584.2007.00374.x.

613 Johnson, D., J. Koplik, and L. Schwartz, (1986), New Pore-Size Parameter Characterizing
614 Transport in Porous Media, Physical Review Letters, 57(20), 2564–2567, doi:
615 10.1103/PhysRevLett.57.2564.

616 Katz, A., and A. Thompson, (1986), Quantitative Prediction of Permeability in Porous Rock,
617 Physical Review. B, Condensed Matter, 34(11), 8179–8181, doi:
618 10.1103/PhysRevB.34.8179.

619 Keating, K, and R. Knight, (2007), A Laboratory Study to Determine the Effect of Iron Oxides
620 on Proton NMR Measurements, Geophysics, 72(1), E27–E32, doi: 10.1190/1.2399445.

621 Keating, K., and R. Knight (2012), The effect of spatial variation in surface relaxivity on nuclear
622 magnetic resonance relaxation rates, Geophysics, 77(5), E365–E377, doi:10.1190/geo2011-
623 0462.1.

624 Keery, J., A. Binley, A. Elshenawy, and J. Clifford, (2012), Markov-chain Monte Carlo
625 estimation of distributed Debye relaxations in spectral induced polarization, Geophysics,
626 77(2), E159, doi: 10.1190/geo2011-0244.1.

627 Kleinberg, R., and M. Horsfield, (1990), Transverse Relaxation Processes in Porous Sedimentary
628 Rock, Journal of Magnetic Resonance, 88(1), 9–19, doi: 10.1016/0022-2364(90)90104-H.

629 Klinkenberg, L. J. (1941), The permeability of porous media to liquids and gases, in Drilling and
630 Production Practice, pp. 200–213, Am. Pet. Inst., N. Y..

631 Knight, R., D. O. Walsh, J. J. Butler, E. Grunewald, G. Liu, A. D. Parsekian, E. C. Reboulet, S.
632 Knobbe, and M. Barrows (2015), NMR Logging to Estimate Hydraulic Conductivity in
633 Unconsolidated Aquifers, Groundwater, 54, 104–114, doi:10.1111/gwat.12324.

634

635 Kruschwitz, S. F. (2008), Assessment of the complex resistivity behavior of salt affected
636 building materials, PhD Thesis, Technical University of Berlin, Berlin, Germany.

637 Kruschwitz, S., A. Binley, D. Lesmes, and A. Elshenawy, (2010), Textural Controls on Low-
638 Frequency Electrical Spectra of Porous Media, Geophysics, 75(4), WA113–WA123, doi:
639 10.1190/1.3479835.

640 Leroy, P., A. Revil, A. Kemna, P. Cosenza, and A. Ghorbani, (2008), Complex conductivity of
641 water-saturated packs of glass beads, Journal of Colloid and Interface Science, 321(1), 103–
642 17, doi: 10.1016/j.jcis.2007.12.031.

643 Marschall, D., J. S. Gardner, D. Mardon, and G. R. Coates (1995), Method for correlating NMR
644 relaxometry and mercury injection data, in *Society of Core Analysts*, p. 9511.

645 Mejus, L., (2015), Using multiple geophysical techniques for improved assessment of aquifer
646 vulnerability, Unpublished PhD thesis, Lancaster Environment Centre, Lancaster
647 University, Lancaster, UK.

648 Morriss, C.E., J. Maclnnis, R. Freedman, J. Smaardyk, C. Straley, W. E. Kenyon, H. S. Vinegar,
649 P. N. Tutunjian, (1993), Field Test Of An Experimental Pulsed Nuclear Magnetism Tool,
650 34th Annual Symposium SPWLA , Calgary, Canada

651 Niu, Q., and A. Revil, (2016), Connecting complex conductivity spectra to mercury porosimetry
652 of sedimentary rocks, Geophysics, 81(1), E17–E32, doi:10.1190/geo2015-0072.1.

653 Nordsiek, S., and A. Weller, (2008), A New Approach to Fitting Induced-Polarization Spectra,
654 Geophysics, 73(6), F235–F245, doi: 10.1190/1.2987412.

655 Purcell, W. R., (1949), Capillary pressures- their measurement using mercury and the calculation
656 of permeability therefrom, Society of Petroleum Engineers, 1(2)39-48 doi:
657 10.2118/94029-G.

658 Revil, A., and N. Florsch (2010), Determination of permeability from spectral induced
659 polarization in granular media, Geophys. J. Int., 181, 1480–1498, doi:10.1111/j.1365-
660 246X.2010.04573.x.

661 Revil, A. (2012), Spectral induced polarization of shaly sands: Influence of the electrical double
662 layer, Water Resour. Res., 48(2), W02517, doi:10.1029/2011WR011260.

663 Revil, A. (2013a), On charge accumulation in heterogeneous porous rocks under the influence of
664 an external electric field, Geophysics, 78(4), D271–D291, doi: DOI 10.1190/GEO2012-0503.1.

665 Revil, A., (2013b), Effective Conductivity and Permittivity of Unsaturated Porous Materials in
666 the Frequency Range 1 mHz-1GHz, Water Resources Research, 49(1), 306–327, doi:
667 10.1029/2012WR012700.

668 Revil, A., N. Florsch, and C. Camerlynck. (2014), Spectral Induced Polarization Porosimetry,
669 Geophysical Journal International, 198(2), 1016–1033, doi: 10.1093/gji/ggu180.

Revil, A., A. Binley, L. Mejus, and P. Kessouri, (2015), Predicting permeability from the characteristic relaxation time and intrinsic formation factor of complex conductivity spectra, Water Resources Research, 51, 1–29, doi: 10.1002/2015WR017074.

Scott, J., and R. Barker, (2003), Determining Pore-Throat Size in Permo-Triassic Sandstones from Low-Frequency Electrical Spectroscopy, Geophysical Research Letters, 30(9), 1450, doi: 10.1029/2003GL016951.

Schoenfelder, W., H. R. Gläser, I. Mitreiter, and F. Stallmach (2008), Two-dimensional NMR relaxometry study of pore space characteristics of carbonate rocks from a Permian aquifer, J. Appl. Geophys., 65(1), 21–29, doi:10.1016/j.jappgeo.2008.03.005.

Slater, L., D. Glaser, (2003), Controls on induced polarization in sandy unconsolidated sediments and application to aquifer characterization, Geophysics, 68(5), 1547–1558, doi: 10.1190/1.1620628.

Schwarz, G., (1962), A Theory of the Low-Frequency Dielectric Dispersion of Colloidal Particles in Electrolyte Solution, Journal of Physical Chemistry, 66, 2636–2642.

Stookey, L., (1970), Ferrozine—a new spectrophotometric reagent for iron, Analytical Chemistry, 42(7), 779–781.

Straley, C., D. Rossini, H. Vinegar, P. Tutunjian, C. Morriss, (1994), Core Analysis by Low Field NMR. Paper presented at 1994 International Symposium, paper SCA- 9404, Society of Core Analysts, Stavanger, Norway.

689 Timur, A. (1969), Pulsed Nuclear Magnetic Resonance Studies of Porostity, Movable Fluid, and
690 Permeability of Sandstones, J. Pet. Technol., 775–786.

691 Vinegar, H. J., and M. Waxman, (1984), Induced Polarization of Shaly Sands, Geophysics,
692 49(8), 1267–1287, doi: 10.1190/1.1441755.

693 Weller, A., S. Nordsiek, and W. Debschütz, (2010), Estimating Permeability of Sandstone
694 Samples by Nuclear Magnetic Resonance and Spectral-Induced Polarization, Geophysics,
695 75(6), E215–E226, doi: 10.1190/1.3507304.

696

697 Weller, A., L. Slater, and S. Nordsiek, (2013), On the Relationship between Induced Polarization
698 and Surface Conductivity : Implications for Petrophysical Interpretation of Electrical
699 Measurements, Geophysics, 78(5), D315–D325, doi: 10.1190/geo2013-0076.

700 Weller, A., L. Slater, A. Binley, S. Nordsiek, and S. Xu (2015), Permeability prediction based on
701 induced polarization : Insights from measurements on sandstone and unconsolidated
702 samples spanning a wide permeability range, Geophysics, 80(2), D161–D173, doi:
703 10.1190/GEO2014-0368.1.

704 Whittall K., M. Bronskill, and R. Henkelman, (1991), Investigation of analysis techniques for
705 complicated NMR relaxation data, Journal of Magnetic Resonance 95(2), 221–234.

706 Zimmermann, E., A. Kemna, J. Berwix, W. Glaas, and H. Vereecken, (2008), EIT Measurement
707 System with High Phase Accuracy for the Imaging of Spectral Induced Polarization

708 Properties of Soils and Sediments, Measurement Science and Technology, 19(9), 094010,
709 doi: 10.1088/0957-0233/19/9/094010.

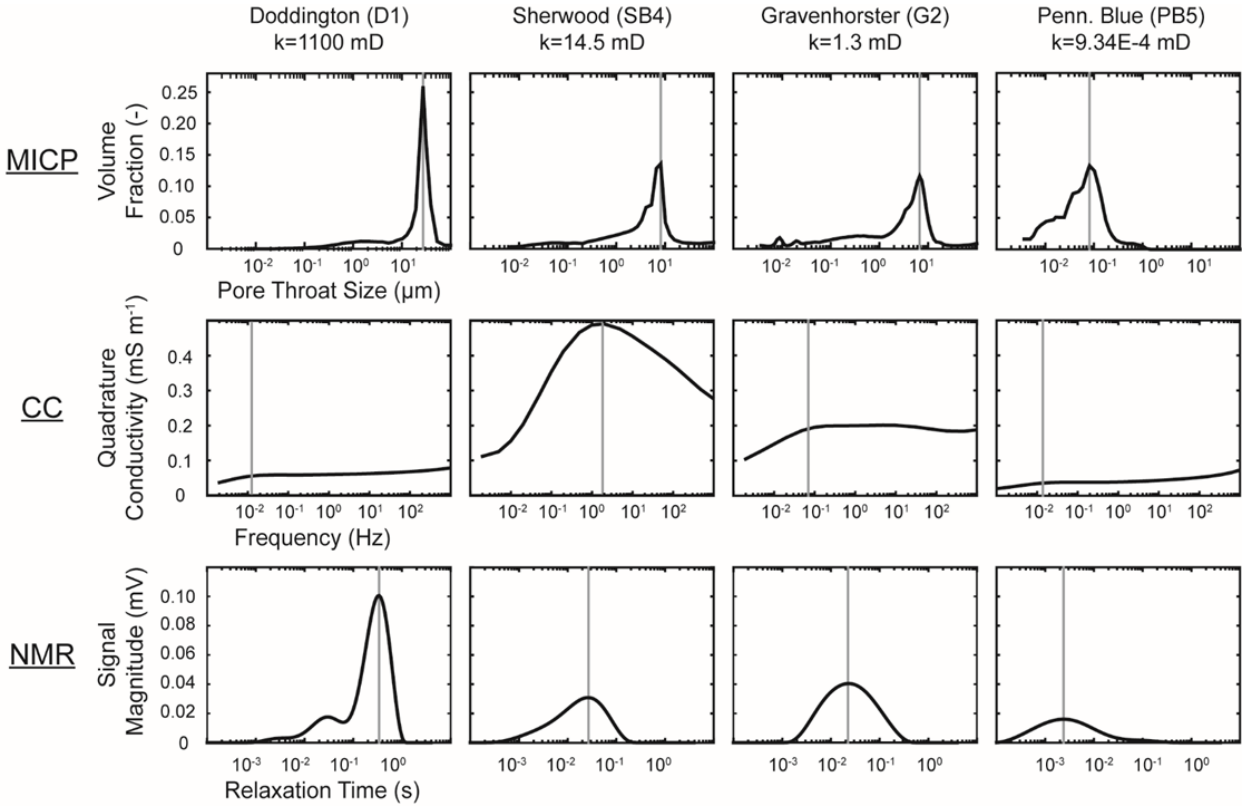

710

711 Figure 1: MICP pore-throat-size distributions, CC imaginary conductivity spectra and NMR T_2
712 distributions for four cores. The Doddington core (D1) represents our high-permeability
713 endmember, the Gravenhorster (G2) and Sherwood (SB4) cores represent the middle range of
714 permeabilities, and the Pennsylvania Blue core (PB5) represents the lowest permeability
715 endmember. The gray lines are the characteristic values chosen to represent each distribution: R_p,
716 the pore throat size associated with the peak in the MICP distribution, f_p, the characteristic
717 frequency used to calculate the characteristic CC relaxation time and T_{2p}, the NMR relaxation
718 time associated with the peak of the distribution.

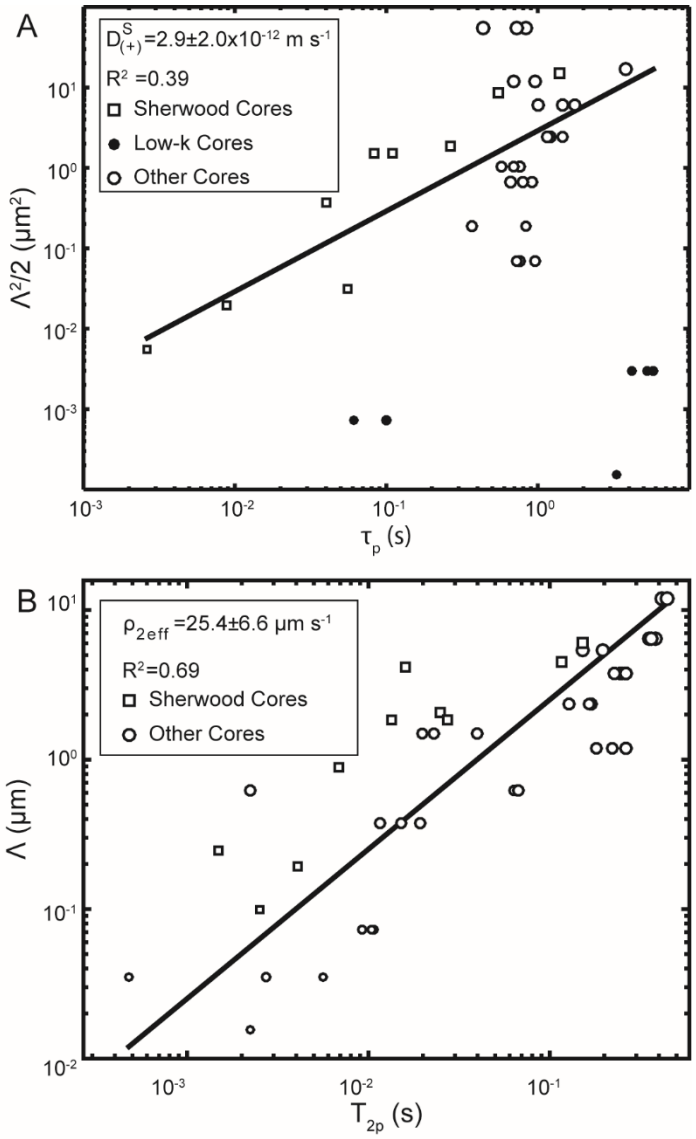

719

720 Figure 2: A) Relationship between τ_p from CC spectra and $\Lambda^2/2$ from the peak of the MICP
721 distributions, given in equation (7) and B) Relationship between T_{2p} from NMR relaxation time
722 distributions and Λ from equation (10). The size of the data points are proportional to log(k) for
723 each core. The solid lines are the linear regressions; in A) the regression is performed on all data
724 except cores from the Arizona Chocolate (AC), Pennsylvania Blue (PB) and Tennessee
725 formations (denoted with filled black circles). Note that the data are not plotted to strictly reflect

726 equations (7) and (10), but have been rearranged so that the slopes of the fitted lines give the
727 value of the respective fitting factors.

728

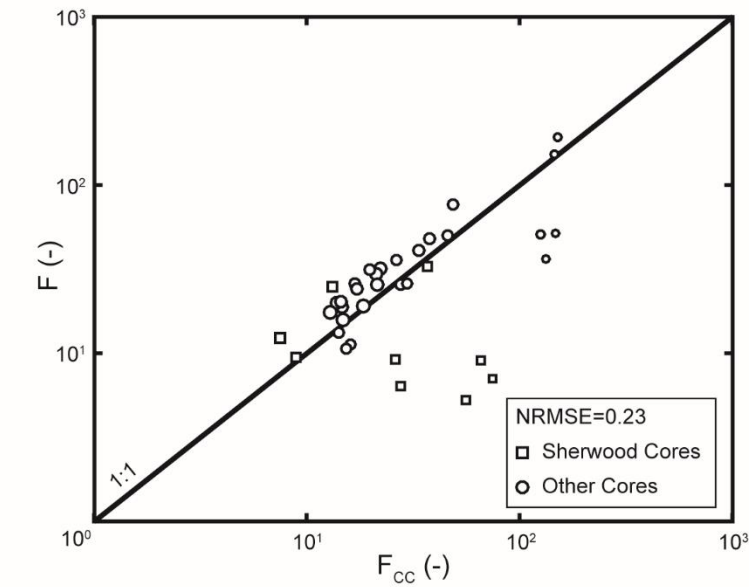

729

730 Figure 3: The intrinsic formation factor calculated from multi-salinity measurements, *F*, plotted
731 against the estimated *F* from CC measurements using equation (5), F_{CC}. The size of the data
732 points are proportional to log(*k*) for each core. The solid line is the 1:1 line.

733

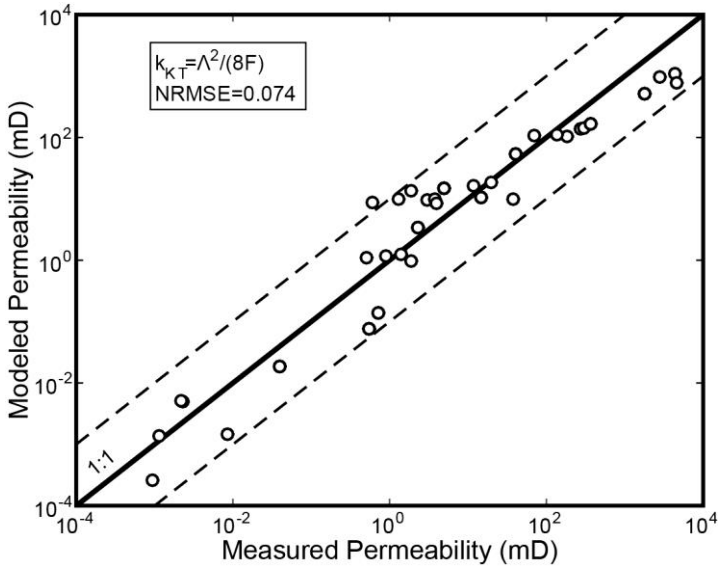

734

735 Figure 4: Permeability modeled using the Katz and Thompson model from equation (2) versus
736 the measured permeability. Modeled permeability uses Λ from MICP measurements and F from
737 multi-salinity measurements. The solid line is the 1:1 line; the dashed lines are the +/- one order
738 of magnitude bounds.

739

740

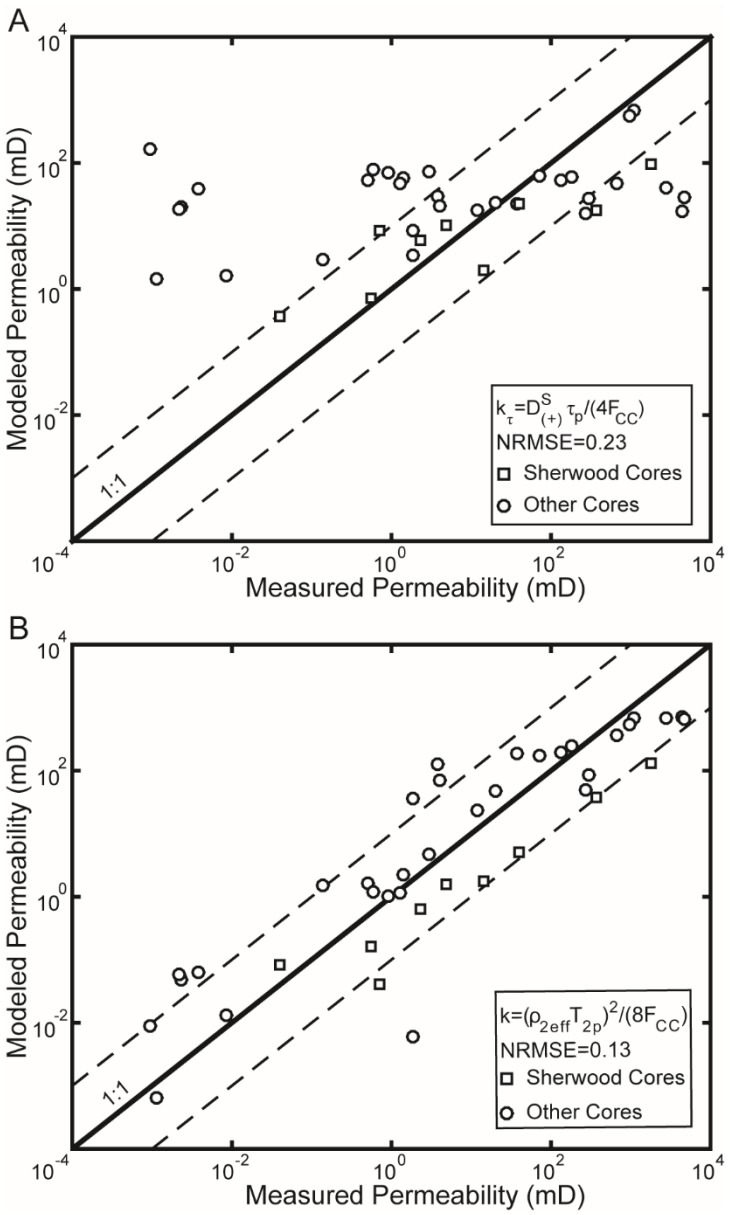

741

742 Figure 5: Modeled permeability versus measured permeability. A and B show the estimates of *k*
743 determined using equations (11) and (12), respectively. The solid line is the 1:1 line; the dashed
744 lines are the +/- one order of magnitude bounds.

745

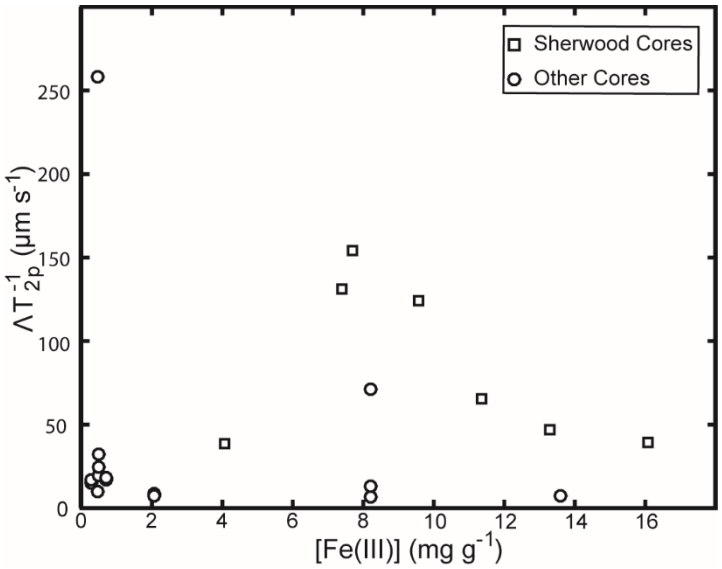

746

747 Figure 6: Fe(III) content plotted against Λ/T_{2p} ($=\rho_{2eff}$). Measurements to determine the Fe(III)

748 content were made on a subsample of a subset of the formations (Arizona Chocolate, Berea,

749 Cottaer, Coconino, Doddington, Tennessee, Sherwood, and Pennsylvania Blue formations).

750

Table 1: Physical properties of all sandstones: dynamically interconnected pore size determined from the peak of MICP pore-throat size distributions (Λ), gas-permeability (*k*) and Fe(III) content are reported. With the exception of the Sherwood cores, Λ was measured on an extra material from each formation rather than for each core individually. Fe(III) data were also collected on a representative sample from each formation except for the Sherwood cores, which were subsampled to provide sample material. Footnotes refer to data acquired and reported. Unavailable data are indicated by (--).

Name	Sample ID	Λ (μm)	*k* (mD)	[Fe(III)] (mg/g)
Arizona Chocolate	AC2	0.04[1]	$1.5x10^{-3}$	8.29
	AC3		$9.7x10^{-4}$	
	AC4		$8.42x10^{-3}$	
Berea	B4	3.48[1]	184	0.33
	B5		135	
	B10		90.4	
	B11		70.7	
Bentheimer	Be1	4.88[2]	270	--
	Be7		298	
Cottaer	C1	0.37[2]	1.40	0.52
	C7		0.511	
	C33		0.900	
Clashach	Clash1	--	663	--
Coconino	Co4	0.61[1]	0.137	0.51
	Co7		1.86	
	Co8		2.65	
Doddington	D1	5.82	1100	0.75
	D2		951	
	D3		896	
Elb	E3	10.53[3]	2770	--
	E6		4360	
	E7		4620	
Gravenhorster	G2	1.43[3]	1.30	--
	G4		3.00	
	G5		0.595	
Island Rust	IR01	2.20[1]	11.8	--
	IR02		19.9	
	IR04		18.7	
Obernkirchener	O3	1.15[3]	3.76	--
	O5		37.8	
	O6		3.99	
Pennsylvania Blue	PB5	0.02[3]	$9.34x10^{-4}$	13.69
Sherwood	HEC18-7	1.94[4]	40.1[4]	--
	VEC15-5	3.86[4]	18.3[4]	--

	VEG2RI-2	5.48[4]	1780[4]	--
	SB1	4.14	366[5]	4.09
	SB2	1.75	4.9[5]	7.44
	SB3	0.87	2.32[5]	9.6
	SB4	1.75	14.5[5]	11.4
	SB5	0.20	0.55[5]	13.31
	SB6	0.10	0.04[5]	16.12
	SB7	0.25	0.71[5]	7.73
Tennessee	T1	0.08[1]	3.84×10^{-3}	2.11
	T2		2.29×10^{-3}	
	T5		2.18×10^{-3}	

[1] *Baker* [2001]; [2] *Kruschwitz* [2008]; [3] *Kruschwitz et al.* [2010]; [4] *Binley et al.* [2005]; [5] *Mejus* [2015]

758

759 Table 2: Table of the measured geophysical properties of the sandstone cores: formation factor
760 (F), CC relaxation time (τ_p) and NMR peak relaxation time (T_{2p}). Unavailable data are indicated
761 by (--).

Formation Name	Sample ID	F (-)	F_{CC}	τ_p (s)	T_{2p} (ms)
Arizona Chocolate	AC2	134.10	36.40	0.07	0.3
	AC3	--	--	--	5.75
	AC4	126.19	51.06	0.12	2.87
Berea	B4	14.59	18.76	1.52	237.14
	B5	13.68	20.03	1.45	220.67
	B10	--	--	--	237.14
	B11	14.40	20.03	1.75	205.35
Bentheimer	Be1	21.94	31.83	0.69	139.91
	Be7	21.10	29.64	1.10	177.83
Cottaer	C1	13.99	13.28	1.05	19.11
	C7	15.90	11.16	0.79	15.03
	C33	15.24	10.54	1.00	11.55
Clashach	Clash1	21.28	25.43	1.67	339.82
Coconino	Co4	--	198.38	0.80	60.43
	Co7	48.75	77.41	0.36	2.37
	Co8	--	--	--	69.40
Doddington	D1	--	13.69	12.73	339.82
	D2	--	15.15	11.51	316.23
	D3	--	--	--	323.90
Elb	E3	14.76	15.70	0.87	365.17
	E6	12.85	17.36	0.40	392.42
	E7	18.37	18.96	0.73	392.42
Gravenhorster	G2	26.20	35.65	2.27	22.0
	G4	27.52	25.40	2.51	38.31
	G5	29.52	26.01	2.77	19.57
Island Rust	IR01	37.48	47.97	1.15	118.28
	IR02	33.38	40.96	1.32	153.99
	IR04	45.75	50.19	0.58	150.34
Obernkirchener	O3	16.75	25.92	1.05	200.49
	O5	17.08	24.02	0.73	237.14
	O6	19.55	31.36	0.87	165.48
Pennsylvania Blue	PB5	148.54	51.80	11.52	2.37
Sherwood	HEC18-7	8.79	9.39	0.29	24.29
	VEC15-5	--	--	--	15.77
	VEG2RI-2	7.42	12.30	1.59	139.91
	SB1	13.07	24.96	0.61	107.46
	SB2	26.1	9.19	0.13	13.34
	SB3	27.64	6.31	0.05	6.98
	SB4	36.97	32.99	0.09	26.74
	SB5	65.46	9.01	8.75×10^{-3}	4.22
	SB6	74.77	6.99	3.48×10^{-3}	2.67
	SB7	55.95	5.22	0.06	1.62
Tennessee	T1	--	112.66	6.05	9.31
	T2	151.79	293.55	5.27	10.75
	T5	146.00	153.99	3.82	10.49

762